

Correlated mass, energy, and angular distributions from bremsstrahlung-induced fission of ^{234}U and ^{232}Th in the energy region of the fission barrier

A. Gök, ^{1,*} C. Eckardt, ¹ J. Enders, ^{1,†} M. Freudenberger, ¹ A. Oberstedt, ² and S. Oberstedt ³

¹*Institut für Kernphysik, Technische Universität Darmstadt, 64289 Darmstadt, Germany*

²*Extreme Light Infrastructure—Nuclear Physics (ELI-NP)/Horia Hulubei National Institute for Physics and Nuclear Engineering (IFIN-HH), 077125 Bucharest-Magurele, Romania*

³*European Commission, DG Joint Research Centre, Directorate G—Nuclear Safety and Security, Unit G.2 Standards for Nuclear Safety, Security and Safeguards, 2440 Geel, Belgium*

(Received 13 March 2017; published 2 October 2017)

The bremsstrahlung-induced fission of ^{234}U and ^{232}Th has been studied at the superconducting Darmstadt linear accelerator (S-DALINAC) in the excitation energy region close to the fission barrier. Fission-fragment mass and total kinetic energy (TKE) distributions from ^{234}U were studied for the first time in this energy region. The results have been analysed in terms of fission modes, and a dominant yield of the mass-asymmetric standard-2 mode was found in both nuclei. No strong dependence of the fission-mode weights on the excitation energy of the compound nucleus was found. Correlations among mass, TKE, and angular distributions have also been investigated. A correlation in the form of an increased anisotropy for far-asymmetric masses and low TKE were found in both fissioning systems. A possible interpretation of this correlation in terms of fission modes is discussed.

DOI: [10.1103/PhysRevC.96.044301](https://doi.org/10.1103/PhysRevC.96.044301)

I. INTRODUCTION

While nuclear fission was discovered more than 75 years ago, the intricacies of the complex process are still not precisely known. In spite of the availability of microscopic descriptions of nuclear fission, phenomenological approaches are still widely used to describe the experimental data. Experimentally, neutron-induced fission reactions have been studied over a wide range of energies in many actinide nuclei. In contrast, the excitation of the fissioning compound nucleus using real photons has been studied in much fewer cases. In this work we have studied the mass, total kinetic energy (TKE) and angular distributions of fission fragments from (γ, f) reactions on ^{234}U and ^{232}Th . Fission induced by real photons represents an important tool to investigate fission barrier structures. This is because near barrier fission proceeds through a few low-lying excitations, the so-called transition states [1]. Measurement of the fission fragment angular distribution allows the identification of the J^π and K characteristic quantum numbers of transition states on top of the inner and outer fission barriers. The absorption of real photons takes place mainly as an electric dipole ($E1$) excitation offering low-energy photofission of even-even nuclei the advantage of spin selectivity. The sequence of transition states on top of the fission barrier is sensitive to the barrier structure and is reflected in the angular distribution of fission fragments. If there exist different paths through the landscape of the fission barrier, leading to different mass splits, then one may expect differences in the available transition states for these paths and thereby a correlation between fission-fragment mass and

angular distributions. Such correlations have been found to exist in photofission [2,3].

Among the stable and long-lived nuclides in the actinide region, the nuclei ^{232}Th and ^{234}U are of a certain interest for an accurate determination of their fission properties following photoexcitation due to possible technical applications in thorium-fueled reactors. Here, the breeder material ^{232}Th may undergo photon-induced fission due to the γ rays inside the reactor, while the (neutron-)fissile nuclide ^{233}U forms a ^{234}U compound nucleus in the (n, f) process.

We report on systematic studies of fission fragment characteristics, including mass and angular-distribution correlations, in the $^{234}\text{U}(\gamma, f)$ and $^{232}\text{Th}(\gamma, f)$ reactions. Fission-fragment mass and TKE distributions are interpreted in terms of the so-called multi-modal random neck rupture (MM-RNR) model [4].

II. EXPERIMENT

Correlated fission-fragment mass, TKE and angular distributions were obtained from the reaction $^{234}\text{U}(\gamma, f)$ using bremsstrahlung of end-point energies $E_0 = 9.0$ MeV, 7.5 MeV, and 6.4 MeV and for the reaction $^{232}\text{Th}(\gamma, f)$ at $E_0 = 9.5$ MeV and 8.0 MeV. For the purpose of calibration, fission-fragment mass and TKE distributions from the reaction $^{238}\text{U}(\gamma, f)$ at $E_0 = 8.5$ MeV were also obtained.

A. Experimental setup

The experiments were performed at the end of the superconducting injector linac of the Superconducting Darmstadt linear accelerator (S-DALINAC [5]). The experimental setup was the same as in our previous experiment [6]. The S-DALINAC electron beam was used to produce bremsstrahlung in a thick copper radiator [7,8]. The fission targets consisted of UF_4 and ThF_4 , respectively, vacuum-evaporated onto one side of thin

*Present address: European Commission, DG Joint Research Centre, Directorate G—Nuclear Safety and Security, Unit G.2 Standards for Nuclear Safety, Security and Safeguards, 2440 Geel, Belgium.

†Corresponding author: enders@ikp.tu-darmstadt.de

TABLE I. Summary of the performed experiments. The first column gives the target nucleus, and the second and third columns give the thickness of target layer and polyimide backing, respectively. The electron beam energy E_0 , the average current $\langle I \rangle$, the beam time T for each measurement, and the number of events NEV accepted in the analysis for the fission-fragment mass and TKE distributions are given in the following columns.

Target nucleus	Target thickness ($\mu\text{g}/\text{cm}^2$)	Polyimide ($\mu\text{g}/\text{cm}^2$)	E_0 (MeV)	$\langle I \rangle$ (μA)	T (h)	NEV
^{234}U	46.6 ± 0.3	32.0 ± 1.5	9.0	23	21	28 185
			7.5	12	96	16 411
			6.4	29	81	3 541
^{232}Th	87.0 ± 5.0	35.2 ± 0.7	9.5	15	22	47 957
			8.0	20	29	15 434
^{238}U	82.9 ± 4.2	35.0 ± 3.0	8.5	18	22	46 715

polyimide foils, with gold layers ($50 \mu\text{g}/\text{cm}^2$) evaporated onto the opposite side. Properties of the targets used in the experiments are summarized in Table I. The fission fragment detector was a twin Frisch-grid ionization chamber (FGIC) [9]. The detector consists of two ionization chambers placed back to back on a common cathode. The fission target is placed in a

hole in the common cathode, allowing for coincident detection of the two fission fragments. The cathode-grid distance was 3 cm, while the grid-anode distance was 0.5 cm. The volume between the electrodes was filled with P-10 gas (90% Ar + 10% CH_4) at a pressure of 1.05 bar, continuously flowing through the chamber at a flow rate of about 60 ml/min. The Frisch-grids were kept at ground potential, and the operating voltage for the cathode (-1.6 kV) was chosen in order to ensure stability of the pulse-height defect [10] and electron drift velocity [11] for small variations in reduced field strength. The operating voltages for the anodes ($+1.0$ kV) were chosen to avoid collection of electrons on the grid [12]. The ionization chamber's symmetry axis (perpendicular to the electrode plane) was oriented along the bremsstrahlung beam, thereby the fission fragment emission angle that could be extracted from the drift time of ionization electrons [13] coincided with the fission axis orientation relative to the photon momentum.

B. Data analysis

The use of bremsstrahlung leads to a continuous distribution of excitation energies of the fissioning nucleus for each electron-beam energy E_0 . It is necessary during the data

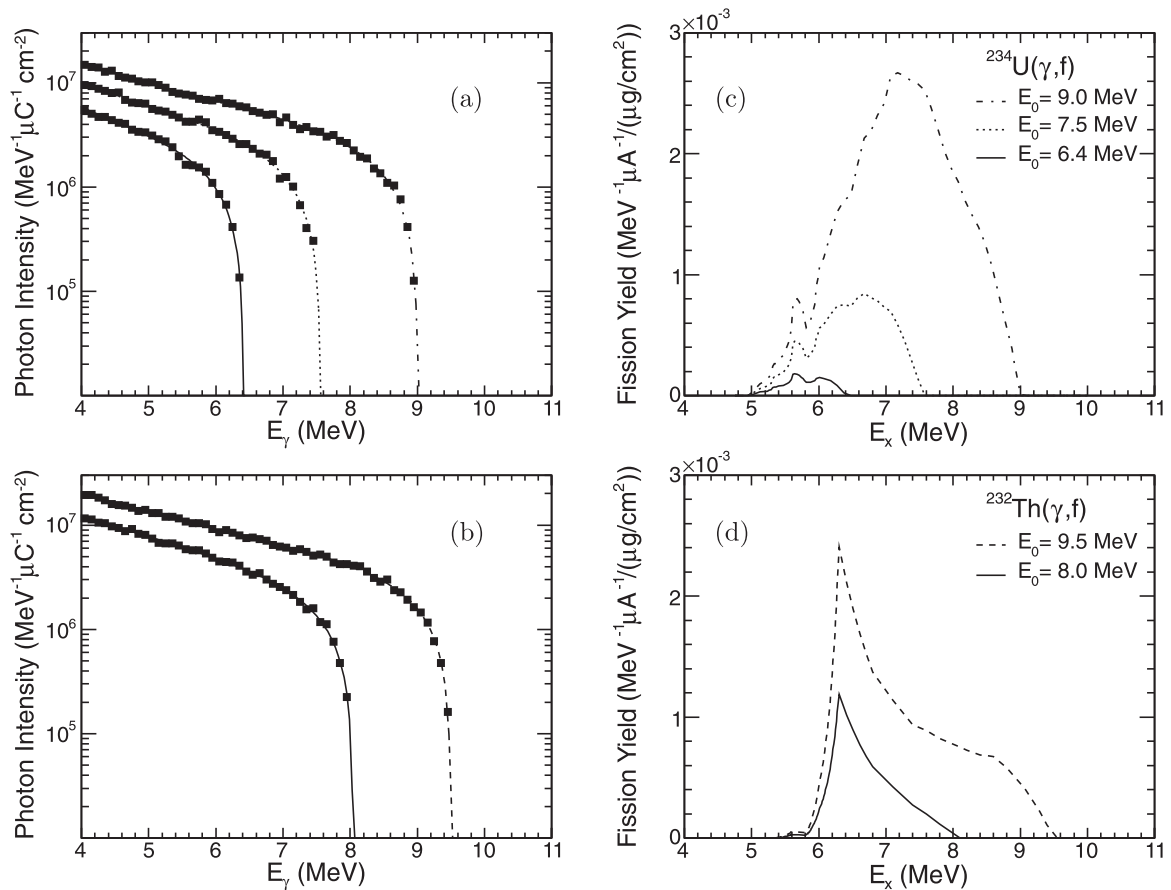


FIG. 1. Bremsstrahlung spectra with endpoint energies of 9.0, 7.5, and 6.4 MeV (a), and 9.5 and 8.0 MeV (b). The solid, dashed, and dotted-dashed lines represent polynomial fits to the data simulated with GEANT4 [14], represented by the black squares. Also shown are corresponding calculated fission yields per μA electron beam current and per $\mu\text{g}/\text{cm}^2$ fission target mass thickness for ^{234}U (c) and for ^{232}Th (d) using cross sections from Refs. [15,16].

analysis to have an estimate of the average excitation energy (E_x) of the fission nucleus. This was calculated from the convolution of bremsstrahlung spectra simulated using Geant4 [14] and photofission cross sections, taken from Refs. [15,16]. In Fig. 1 the simulated bremsstrahlung spectra and the resulting excitation energy spectra are displayed.

The determination of fission-fragment masses is based on the well-established double kinetic energy ($2E$) technique. Conservation of linear momentum, with the approximation that the sum of the two fission-fragment masses is equal to the mass of the fissioning nucleus, leads to the following relation:

$$A_{1,2} = A_f \frac{E_{2,1}}{\text{TKE}}, \quad (1)$$

for fission fragments entering chamber side (1) and (2), respectively. The masses have been replaced by the corresponding mass numbers $A_{1,2}$, $E_{1,2}$ are the fragments' kinetic energies, $\text{TKE} = E_1 + E_2$ is the total kinetic energy, and A_f is the mass number of the fissioning nucleus. For a correct determination of the energies, the energy loss in the target needs to be accounted for. The energy loss depends on the distance a fragment has to travel inside the solid sample before entering the sensitive volume, and it therefore depends on the emission angle and whether the fragment exited through the target or the backing side. The emission angle was extracted from the drift time of ionization electrons, which allowed corrections for angle-dependent systematic errors in the pulse-height data. A detailed description of the procedure for determining the emission angles and the subsequent corrections to the pulse height data can be found in Ref. [13]. The $\cos\theta$ resolution, with θ being the angle between fragment track and target normal, was determined from the distribution of the difference in $\cos\theta$ from the two chamber sides. This was done for each target individually with resulting $\cos\theta$ resolutions of 0.070 and 0.067 for the ^{234}U and the ^{232}Th targets, respectively. The pulse-height defect (PHD) of the counting gas was taken into account in calibrating the measurement on ^{238}U at $E_0 = 8.5$ MeV using results on bremsstrahlung-induced fission from Ref. [17], with a parametrization of the PHD according to Ref. [9], in terms of dimensionless Lindhard-Scharff-Schiøtt (LSS) units [18,19].

Because of the change in the fragments' kinetic energies, caused by neutron evaporation, the relation in Eq. (1) is not valid for the detected energies. Assuming that ν neutrons are evaporated isotropically from a fully accelerated fragment, the energies before E_{pre} and after E_{post} neutron evaporation are related according to

$$E_{\text{pre}} = \frac{A}{A - \nu} E_{\text{post}}, \quad (2)$$

where A is the fragment mass number before neutron emission. If ν is known, then the fragment energy and mass before neutron evaporation can be obtained from Eqs. (1) and (2) iteratively, starting from the measured post-neutron energies. The number of evaporated neutrons depends on the fragment's mass and its excitation energy. The average neutron multiplicity as a function of fragment mass $\bar{\nu}(A)$ from Refs. [20,21] was used to account for the mass dependence. The $\bar{\nu}(A)$ distribution was scaled with the average excitation energy of the compound

nucleus to reproduce the average number of neutrons per fission. To take the fragment excitation energy dependence into account, the neutron multiplicity was scaled with the total kinetic energy according to [22]

$$\bar{\nu}(A, \text{TKE}) = \bar{\nu}(A) + \frac{\bar{\nu}(A)}{\bar{\nu}(A) + \bar{\nu}(A_f - A)} \times \frac{\langle \text{TKE} \rangle(A) - \text{TKE}}{8.6 \text{ MeV}}, \quad (3)$$

where 8.6 MeV is the average energy cost to emit a neutron. The average preneutron total kinetic energy as a function of the fragment mass $\langle \text{TKE} \rangle(A)$ is only known once the neutron evaporation has been taken into account. Therefore the analysis is carried out in two steps; in the first step the second term of Eq. (3) is neglected, the resulting $\langle \text{TKE} \rangle(A)$ is then used in the second step to calculate the TKE dependence of the number of evaporated neutrons according to Eq. (3).

III. EXPERIMENTAL RESULTS AND DISCUSSION

In the following, experimental results for $^{234}\text{U}(\gamma, f)$ and $^{232}\text{Th}(\gamma, f)$ are presented and discussed in terms of fission

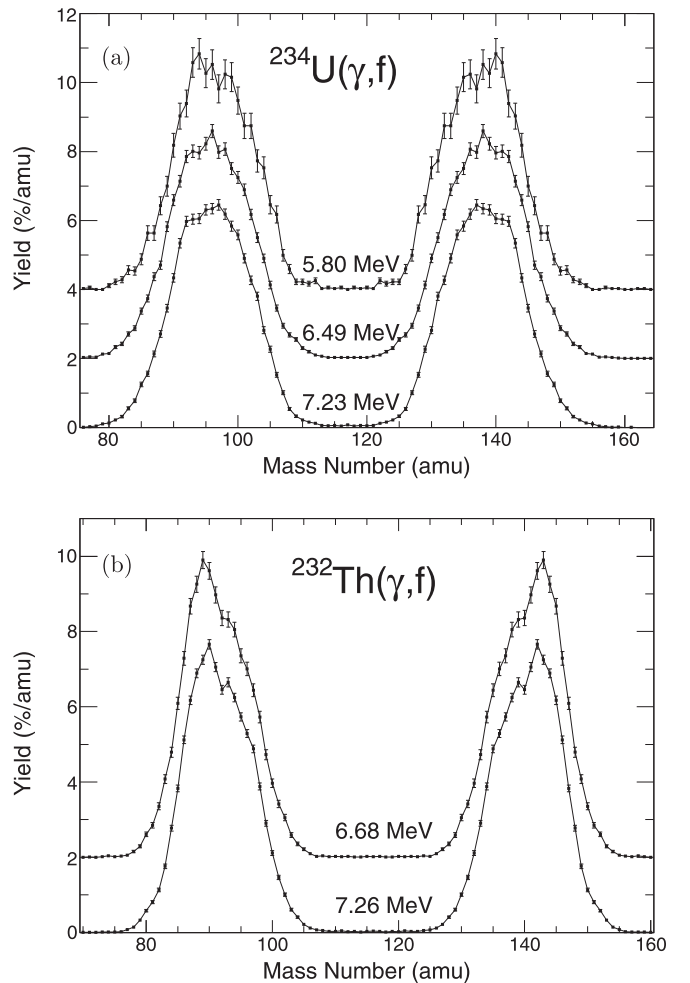


FIG. 2. Fission-fragment mass yield distributions from the reactions $^{234}\text{U}(\gamma, f)$ (a) and $^{232}\text{Th}(\gamma, f)$ (b). The curves are consecutively displaced by 2% and labeled with the average excitation energy.

TABLE II. Characteristic parameters of the measured total kinetic energy and mass distributions from photofission of ^{234}U . The calculated average excitation energy of the fissioning nucleus is denoted by $\langle E_x \rangle$, and σ_{E_x} stands for the standard deviation of the excitation energy. The mean heavy-fragment mass and the standard deviation of the mass peak are denoted by $\langle A_H \rangle$ and σ_A , respectively, and $\langle \text{TKE} \rangle$ indicates the total kinetic energy with standard deviation σ_{TKE} .

E_0 (MeV)	$\langle E_x \rangle$ (MeV)	σ_{E_x} (MeV)	$\langle \text{TKE} \rangle$ (MeV)	σ_{TKE} (MeV)	$\langle A_H \rangle$ (amu)	σ_A (amu)
6.4 ± 0.1	5.80	0.09	169.88 ± 0.12	10.44 ± 0.09	137.77 ± 0.05	5.77 ± 0.04
7.5 ± 0.1	6.49	0.29	170.00 ± 0.08	10.59 ± 0.06	138.29 ± 0.05	5.92 ± 0.03
9.0 ± 0.1	7.23	0.66	169.79 ± 0.05	10.11 ± 0.03	138.10 ± 0.04	5.79 ± 0.03

modes. Unless stated otherwise, uncertainties are statistical ones only.

A. Mass and TKE distributions

The obtained preneutron fission-fragment-mass distributions are displayed in Fig. 2. Characteristic parameters of the mass and TKE distributions are given in Tables II and III for ^{234}U and ^{232}Th , respectively.

The $^{234}\text{U}(\gamma, f)$ fission yields show qualitative agreement with the predictions by Randrup and Möller [23] for an average excitation energy of 6.5 MeV. While the most probable mass is relatively close to the results from the present experiment the distributions from the model calculation are much narrower than the experimental ones, with the most asymmetric fission events being underpredicted. Randrup and Möller used the scaling $P(Z) = P(A) * Z_f/A_f$, where Z_f and A_f are the compound proton and mass numbers, respectively, in order to compare their calculated mass distributions with charge distribution data of Schmidt *et al.* [24], obtained from electromagnetic induced fission in inverse kinematics. Applying the same inverse relation to the data of Schmidt *et al.* [24], one finds very good agreement with the mass distribution from our experiment, both in the mass of the most probable fission fragment as well as the widths of the mass distribution.

The correlated mass and TKE data has been analyzed within the framework of the MM-RNR model [4]. As mentioned earlier, the yield predicted in this model is a superposition of the yields from individual fission modes. To extract information on the characteristics of the involved modes and their relative importance, a fit to the experimentally obtained yield as a function of both fragment mass and TKE is

performed according to the expression

$$Y(A, \text{TKE}) = \sum_m w_m Y_m(A, \text{TKE}),$$

$$Y_m(A, \text{TKE}) = \frac{1}{4\pi\sigma_{A,m}} \left\{ \exp \left[-\frac{(A - \langle A \rangle_m)^2}{2\sigma_{A,m}^2} \right] + \exp \left[-\frac{(A - A_f + \langle A \rangle_m)^2}{2\sigma_{A,m}^2} \right] \right\} \times \left(\frac{200}{\text{TKE}} \right)^2 \exp \left[\frac{-(L - l_{\max,m})^2}{(L - l_{\min,m})l_{\text{dec},m}} \right], \quad (4)$$

where the index m denotes a fission mode and w_m is the fission mode weight. The distance between the fragments' charge centers at scission is denoted by L . Considering only Coulomb interaction, this quantity may be approximated by

$$L = \frac{e^2}{4\pi\epsilon_0} \frac{Z_L Z_H}{\text{TKE}} \approx 1.44 \text{ MeV fm} \left(\frac{Z_f}{A_f} \right)^2 \frac{(A_f - A)A}{\text{TKE}},$$

where Z_L and Z_H are light and heavy fragments' proton numbers, respectively. They were approximated assuming conservation of the charge-to-mass ratio of the fissioning nucleus. The part describing the mass distribution is a simple superposition of two Gaussians, one for the heavy fragment and one for the light fragment. For symmetry reasons both use the same set of parameters for each mode: the mean heavy-fragment mass number $\langle A \rangle_m$ and the width $\sigma_{A,m}$ of the mass yield. The part describing the TKE uses three parameters for the distance between the fragments' charge centers at scission, with the following intuitive meanings:

- (i) The most probable distance is denoted l_{\max} ,

TABLE III. Characteristic parameters of the measured total kinetic energy and mass distributions from photofission of ^{232}Th . The calculated average excitation energy of the fissioning nucleus is denoted by $\langle E_x \rangle$ and σ_{E_x} stands for the standard deviation of the excitation energy. The mean heavy-fragment mass and the standard deviation of the mass peak are denoted by $\langle A_H \rangle$ and σ_A , respectively, and $\langle \text{TKE} \rangle$ indicates the total kinetic energy with standard deviation σ_{TKE} .

E_0 (MeV)	$\langle E_x \rangle$ (MeV)	σ_{E_x} (MeV)	$\langle \text{TKE} \rangle$ (MeV)	σ_{TKE} (MeV)	$\langle A_H \rangle$ (amu)	σ_A (amu)
8.0	6.68	0.22	162.71 ± 0.05	8.84 ± 0.04	140.74 ± 0.04	5.19 ± 0.03
9.5	7.26	0.80	163.39 ± 0.03	8.95 ± 0.02	140.46 ± 0.03	5.23 ± 0.02

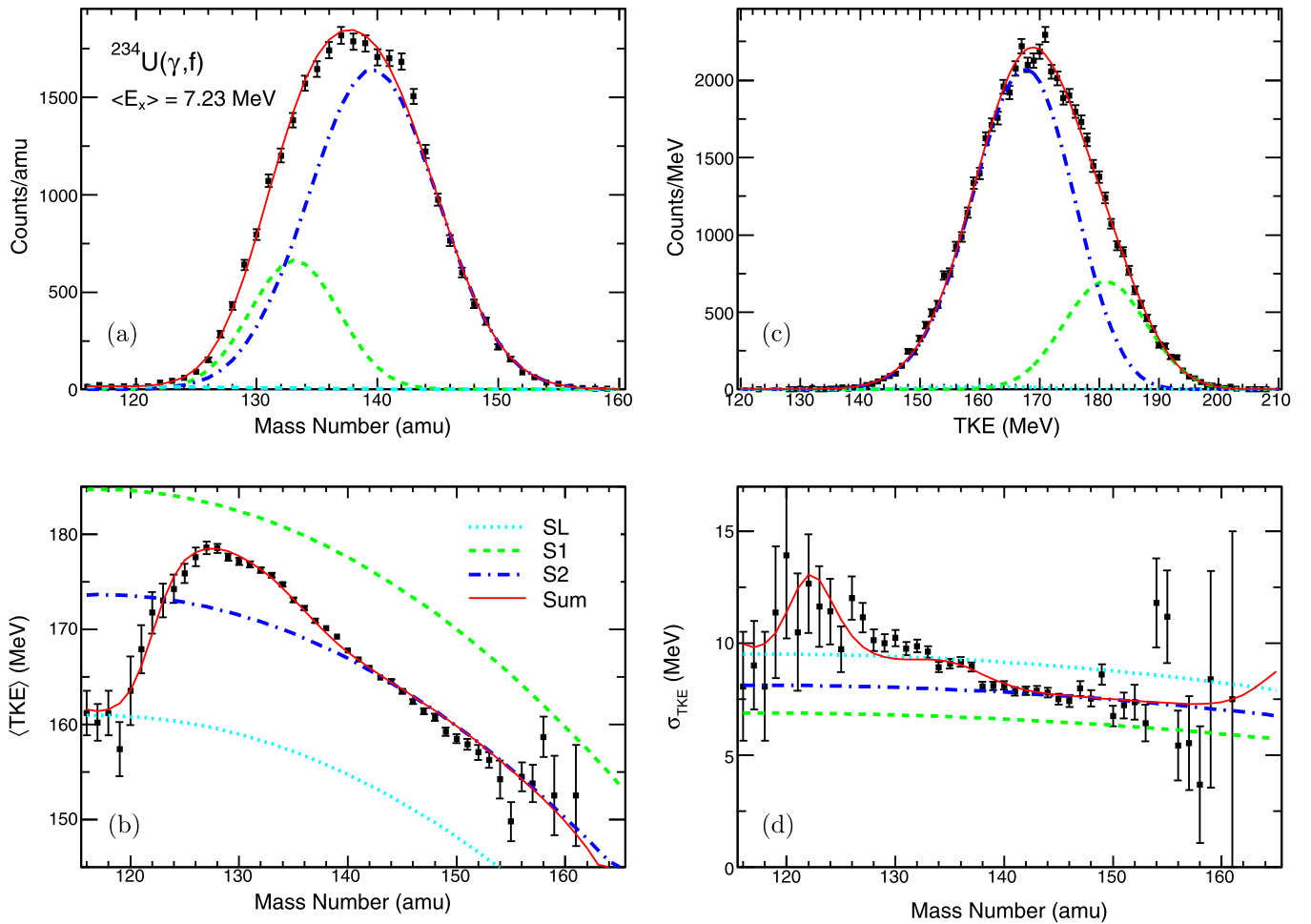


FIG. 3. Yield as a function of heavy-fragment mass number (a) and TKE (c) as well as average TKE (b) and width (d) as function of the fragment mass from $^{234}\text{U}(\gamma, f)$ at $\langle E_x \rangle = 7.23$ MeV. The lines represent results from fits according to Eq. (4). The solid red line corresponds to the weighted sum of the individual fission modes. The individual fission modes are represented by the other, differently colored, lines.

- (ii) the smallest allowed distance, due to Q-value limitation, by l_{\min} , and
- (iii) the exponential decrease in yield with simultaneous increase in L is described by l_{dec} .

In the fission of light actinides three modes are predicted to play a role, the super-long (SL) mode, which is symmetric in mass with low TKE, and the two mass-asymmetric so-called standard modes (S1, S2) centered around the masses 135 and 141, respectively. The total fit-function then has 18 parameters. The fits were performed using the method of maximum log-likelihood and the Minit computer code [25,26].

Results of the fits of Eq. (4) to the experimental data are summarized in Tables IV and V. The mode-weights w_m in Eq. (4) are not strictly proportional to the relative yields Y_m of the fission modes. Both w_m and Y_m are referred to as the mode weight in the literature; for clarity both quantities are therefore given in the Tables. In Figs. 3 and 4, results of the fits are shown for the example of $^{234}\text{U}(\gamma, f)$ at $\langle E_x \rangle = 7.23$ MeV and $^{232}\text{Th}(\gamma, f)$ at $\langle E_x \rangle = 7.26$ MeV, respectively. As is evident in these figures and by the reduced χ^2 values given in Tables IV and V, the individual fits describe the respective experimental data well.

The S1 and S2 modes can be associated with the spherical $N = 82$ and the deformed $N \approx 88$ neutron shells of the scission point model [27], respectively. A systematic behavior of the relative importance of the two standard modes with the neutron number of the fissioning system may therefore be expected. In Fig. 5 the relative yields of the S1 mode Y_{S1} , averaged over the excitation energies is plotted as a function of the neutron numbers of the fissioning nuclei; data from Refs. [28–30] is also included. A systematic behavior is indeed recognized, which can be qualitatively explained by the interplay of the two neutron shells with the spherical proton shell $Z = 50$, cf. Ref. [30]. The increasing yield of the S1 mode with increasing neutron number may be connected with the fact that the larger the neutron number of the fissioning nucleus is, the closer the Z/A ratio comes to that of a doubly magic heavy-fragment with $Z = 50$ and $N = 82$.

B. Influence of energy-loss in the target

Comparing the results obtained in the present experiments to results obtained earlier [6] for the case of $^{234}\text{U}(\gamma, f)$ with the same experimental setup, some discrepancies are observed. The widths of mass and TKE distributions are consistently

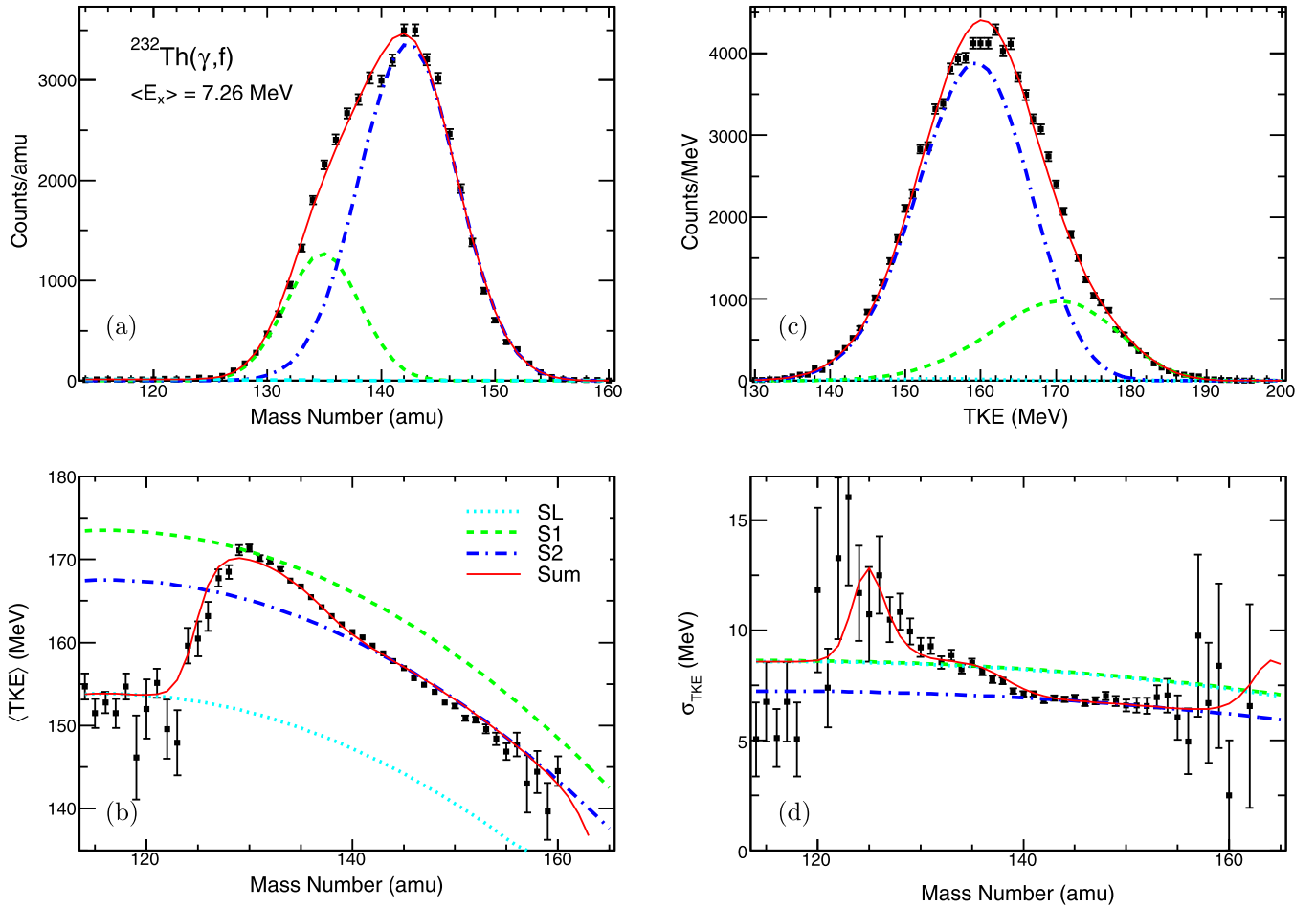


FIG. 4. Yield as a function of heavy-fragment mass number (a) and TKE (c) as well as average TKE (b) and width (d) as function of the fragment mass from $^{232}\text{Th}(\gamma, f)$ at $\langle E_x \rangle = 7.26$ MeV. The lines represent results from fits according to Eq. (4). The solid red line corresponds to the weighted sum of the individual fission modes. The individual fission modes are represented by the other, differently colored, lines.

smaller in the present work. Furthermore, a more pronounced minimum in $\langle \text{TKE} \rangle$ for symmetric mass splits and an increase in the slope of $\langle \text{TKE} \rangle$ as function of fragment mass for asymmetric mass splits are observed in the present results. The

discrepancies also manifest themselves in the results obtained from the fission mode fits; the S1 mode weight is increased by about a factor of two in the present work compared to the results presented in Ref. [6].

TABLE IV. Characteristics of the fission modes from fitting the ^{234}U data to Eq. (4). Given are the average excitation energies of the compound nucleus $\langle E_x \rangle$, the reduced chi squared $\bar{\chi}^2$ of the fit, the relative yield Y and weight w , as well as average heavy-fragment mass number $\langle A_H \rangle$, mass width σ_A , average total kinetic energy $\langle \text{TKE} \rangle$ and total kinetic energy width σ_{TKE} , of the fitted fission modes S1, S2, and SL. Values labeled (*) were kept fixed during the fitting. Also included are theoretical predictions from Ref. [4] of the characteristics.

$\langle E_x \rangle$ (MeV)	$\bar{\chi}^2$		Y (%)	w (%)	$\langle A_H \rangle$ (amu)	σ_A (amu)	$\langle \text{TKE} \rangle$ (MeV)	σ_{TKE} (MeV)
7.23	1.07	S1	25.0 ± 1.7	27.1 ± 1.0	133.1 ± 0.1	3.7 ± 0.1	181.0 ± 0.3	6.9 ± 0.1
		S2	74.5 ± 1.7	72.3 ± 1.4	139.5 ± 0.1	5.3 ± 0.1	166.8 ± 0.1	8.4 ± 0.1
		SL	0.4 ± 0.1	0.6 ± 0.2	117.0*	12.3 ± 2.8	159.1 ± 1.8	9.8 ± 2.3
6.49	1.04	S1	25.8 ± 2.0	30.1 ± 1.4	133.2 ± 0.2	4.1 ± 0.1	180.0 ± 0.4	7.1 ± 0.2
		S2	73.8 ± 2.0	69.5 ± 2.1	140.0 ± 0.2	5.3 ± 0.1	165.8 ± 0.1	9.0 ± 0.1
		SL	0.4 ± 0.1	0.3 ± 0.1	117.0*	11.9 ± 1.7	160.0 ± 2.5	11.8 ± 1.7
5.80	1.04	S1	22.7 ± 2.4	28.8 ± 2.5	132.5 ± 0.3	3.5 ± 0.2	181.3 ± 0.7	7.0 ± 0.4
		S2	76.8 ± 2.6	70.9 ± 2.8	139.3 ± 0.2	5.2 ± 0.1	166.5 ± 0.3	8.6 ± 0.2
		SL	0.5 ± 0.3	0.4 ± 0.2	117.0*	11.9 ± 0.1	161.9 ± 0.4	9.7 ± 0.0

TABLE V. Characteristics of the fission modes from fitting the ^{232}Th data to Eq. (4). Given are the average excitation energies of the compound nucleus $\langle E_x \rangle$, the reduced chi squared $\tilde{\chi}^2$ of the fit, the relative yield Y and weight w , as well as average heavy-fragment mass number $\langle A_H \rangle$, mass width σ_A , average total kinetic energy (TKE) and total kinetic energy width σ_{TKE} , of the fitted fission modes S1, S2, and SL. Values labeled (*) were kept fixed during the fitting. Also included are theoretical predictions from Ref. [4] of the characteristics.

$\langle E_x \rangle$ (MeV)	$\tilde{\chi}^2$		Y (%)	w (%)	$\langle A_H \rangle$ (amu)	σ_A (amu)	$\langle \text{TKE} \rangle$ (MeV)	σ_{TKE} (MeV)
7.26	1.46	S1	22.1 ± 0.9	21.1 ± 0.8	134.8 ± 0.1	3.25 ± 0.05	171.3 ± 0.2	8.7 ± 0.1
		S2	77.4 ± 0.9	78.5 ± 0.9	142.3 ± 0.1	4.29 ± 0.03	161.3 ± 0.1	7.5 ± 0.1
		SL	0.5 ± 0.4	0.42 ± 0.0	116.0*	12.3 ± 2.2	154.3 ± 2.9	9.2 ± 1.6
6.68	1.32	S1	23.0 ± 0.8	18.7 ± 0.7	135.3 ± 0.1	3.71 ± 0.08	170.3 ± 0.2	8.9 ± 0.2
		S2	76.9 ± 1.0	71.7 ± 0.9	142.6 ± 0.1	4.29 ± 0.04	160.8 ± 0.1	7.6 ± 0.1
		SL	0.1 ± 0.3	9.57 ± 26.50	116.0*	8.3 ± 2.92	149.5 ± 3.6	8.9 ± 3.1

These discrepancies may be explained by the difference in the thickness of the active layer of the target used in the two experiments. In the present experiment this thickness was $46.6 \mu\text{g}/\text{cm}^2$, about a factor of four smaller than $190 \mu\text{g}/\text{cm}^2$ in Ref. [6]. In order to quantify this conjecture, a Monte Carlo simulation that convoluted the present result with the resolution of the earlier experiment was performed. When correcting for the energy loss in the target and backing materials a constant specific energy loss must be assumed for all fragments. Furthermore, only the average energy loss as a function of emission angle can be determined. Adding a UF_4 layer of thickness T will introduce an uncertainty in the depth, where the fission takes place inside the target. The energy loss of complementary fragments 1 and 2 in the added layer can be approximated as

$$\Delta E_1 = \left(\frac{1}{\rho} \frac{dE}{dx} \right)_U \frac{d}{\cos \theta} + 4 \frac{m_F}{m_U} \left(\frac{1}{\rho} \frac{dE}{dx} \right)_F \frac{d}{\cos \theta}$$

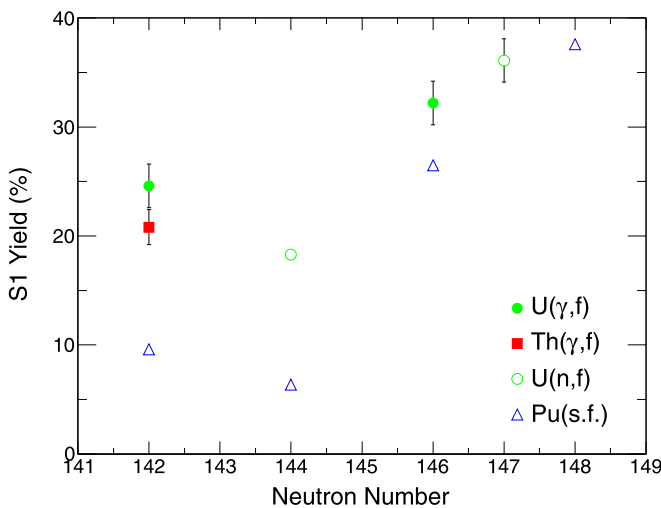


FIG. 5. The relative yield of the S1 mode Y_{S1} averaged over the excitation energies as a function of the neutron number of the compound nucleus. Literature data on neutron-induced fission of ^{235}U [28] and ^{238}U [29] as well as spontaneous fission of four different Pu isotopes [30] is included for comparison.

and

$$\Delta E_2 = \left(\frac{1}{\rho} \frac{dE}{dx} \right)_U \frac{T-d}{\cos \theta} + 4 \frac{m_F}{m_U} \left(\frac{1}{\rho} \frac{dE}{dx} \right)_F \frac{T-d}{\cos \theta}, \quad (5)$$

where d is a depth parameter, see illustration in Fig. 6, while m_F and m_U denote the atomic masses for fluorine and uranium, respectively. To describe the specific energy loss, the Bethe-Bloch formula was used

$$\left(\frac{1}{\rho} \frac{dE}{dx} \right)_X = \kappa_X \frac{Z_X Z_{\text{eff}}^2}{\beta^2} \times \left[\ln \left(\frac{2m_e c^2}{\langle I \rangle_X} \frac{\beta^2}{1-\beta^2} \right) - \beta^2 - \left(\frac{C}{Z} \right)_X \right], \quad (6)$$

where

$$\kappa_X = \frac{3.071 \times 10^{-7}}{A_X} \text{ MeV}/(\mu\text{g}/\text{cm}^2),$$

and Z_X and A_X are proton and mass numbers of the target atom X , respectively, and β is the fragment's relativistic velocity. The mean excitation and ionization potentials $\langle I \rangle_X$ and the shell correction terms $(\frac{C}{Z})_X$ were taken from Ref. [31]. The effective charge was estimated using an empirical expression for fission fragments [32],

$$\frac{Z_{\text{eff}}}{Z} = 1 - (1.034 - 0.177e^{-0.08114Z})e^{-a}, \quad (7)$$

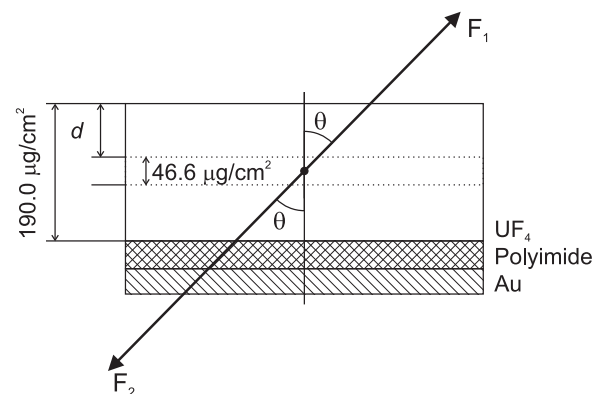


FIG. 6. Illustration of the target composition and the angle-dependent energy loss.

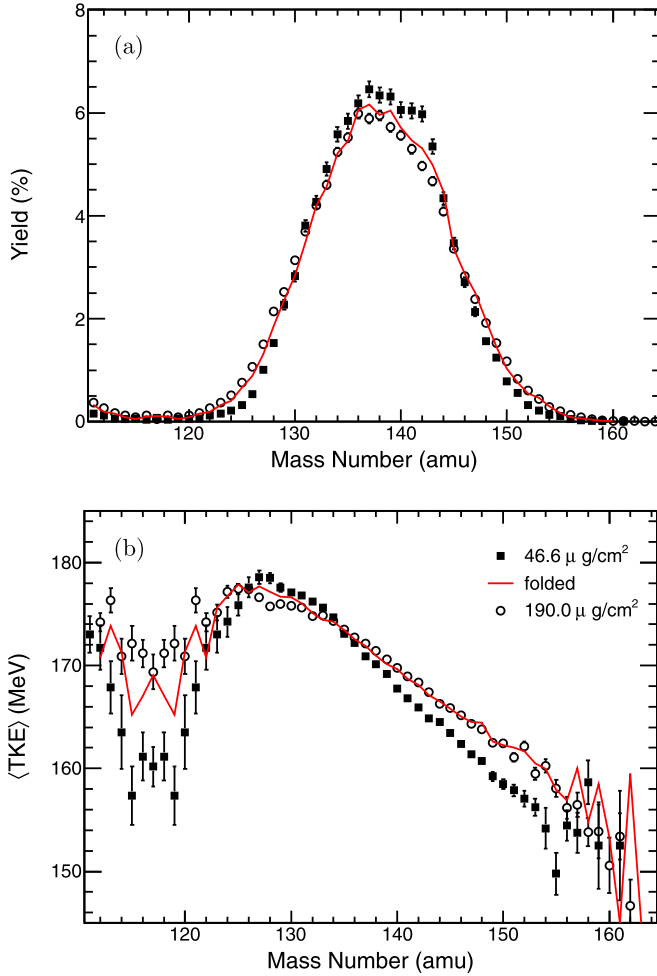


FIG. 7. Fragment yield (a) and average TKE (b) as a function of the fragment mass number for $^{234}\text{U}(\gamma, f)$ at $E_0 = 9.0$ MeV. The open circles represent results obtained with a $190.0 \mu\text{g}/\text{cm}^2$ target [6], full squares represent results obtained in the present experiment with a $46.6 \mu\text{g}/\text{cm}^2$ target. The red line represent the simulated effect of the energy loss in the $190.0 \mu\text{g}/\text{cm}^2$ target on the data obtained with the $46.6 \mu\text{g}/\text{cm}^2$ target.

where

$$a = b + 0.0378 \sin\left(\frac{\pi}{2}b\right) \quad \text{and}$$

$$b = 0.866 \sqrt{\frac{E/\text{keV}}{25A}} Z^{-2/3}.$$

the quantities Z and A are the fragment's charge and mass numbers, respectively, and E its kinetic energy.

The Monte Carlo procedure uses the data of the present experiment on ^{234}U at $E_0 = 9.0$ MeV with the $46.6 \mu\text{g}/\text{cm}^2$ thick target. By randomizing $d \in [0, 143.4] \mu\text{g}/\text{cm}^2$ for each event and using Eq. (5), a new data set is generated that corresponds to the experiment performed earlier with the $190.0 \mu\text{g}/\text{cm}^2$ target. This data set was then reanalyzed according to the procedure described above. The result of this analysis on the mass distribution and $\langle \text{TKE} \rangle$ as a function of fragment mass is presented in Fig. 7, where solid red lines represent the results of the Monte Carlo procedure, while full squares and open circles represent the results of the experiments with the $46.6 \mu\text{g}/\text{cm}^2$ target from this work and the $190.0 \mu\text{g}/\text{cm}^2$ target from Ref. [6], respectively. Obviously, the simulation reproduces the results obtained with the thicker target well.

In Table VI the results of the fit to the data obtained with the $46.6 \mu\text{g}/\text{cm}^2$ target is compared to the fit to the data obtained with the $190.0 \mu\text{g}/\text{cm}^2$ target, with bremsstrahlung of endpoint energy of 9.0 MeV. The fit to the data obtained with the thicker target did not converge when all three fission modes were included, therefore the low yield SL mode had to be excluded from the fit. A smaller weight for the S1 mode is observed for the thicker of the two targets. Also included in Table VI are results of a fit to the data obtained from the Monte Carlo procedure. The result of the fit to the folded data agrees well with the fit to the data obtained with the thicker target, which corroborates the conclusions drawn. It can be concluded that the discrepancies observed for the two experiments on $^{234}\text{U}(\gamma, f)$ are indeed explained by an effect of a deteriorated resolution due to increased energy loss in the earlier experiment. Furthermore, it can be concluded that when performing $2E$ experiments special attention should be

TABLE VI. Comparison of the results of the fits of Eq. (4) obtained in this study with a $46.6 \mu\text{g}/\text{cm}^2$ target and those obtained earlier [6] with a $190.0 \mu\text{g}/\text{cm}^2$ targets. The last rows give results for the simulated effect of the added target thickness. Values marked (*) were kept fixed during the fitting.

Target	$\tilde{\chi}^2$		Yield (%)	w (%)	$\langle A_H \rangle$ (amu)	σ_A (amu)	l_{\max} (fm)	l_{\min} (fm)	l_{dec} (fm)
$46.6 \mu\text{g}/\text{cm}^2$	1.07	S1	25.0 ± 1.7	27.1 ± 1.0	133.1 ± 0.1	3.66 ± 0.07	16.45 ± 0.02	9.0 ± 2.1	0.10 ± 0.04
		S2	74.5 ± 1.7	72.3 ± 1.4	139.5 ± 0.1	5.29 ± 0.05	17.37 ± 0.01	12.9 ± 0.2	0.28 ± 0.01
		SL	0.4 ± 0.1	0.59 ± 0.2	117.0*	12.3 ± 2.8	18.61 ± 0.21	14.1 ± 2.0	0.51 ± 0.20
$190.0 \mu\text{g}/\text{cm}^2$	1.21	S1	12.3 ± 2.2	13.8 ± 1.2	133.6 ± 0.3	4.5 ± 0.2	16.5 ± 0.03	11.8*	0.33 ± 0.01
		S2	87.7 ± 2.2	86.2 ± 1.2	138.40 ± 0.04	6.50 ± 0.03	17.08 ± 0.01	11.8*	0.369 ± 0.003
		SL		0.0*					
Simulation	1.00	S1	8.7 ± 1.8	12.6 ± 0.9	133.5 ± 0.2	3.8 ± 0.2	16.22 ± 0.03	11.8*	0.127 ± 0.01
		S2	91.3 ± 1.8	87.4 ± 0.9	138.57 ± 0.06	6.20 ± 0.03	17.16 ± 0.01	11.8*	0.230 ± 0.003
		SL		0.0*					

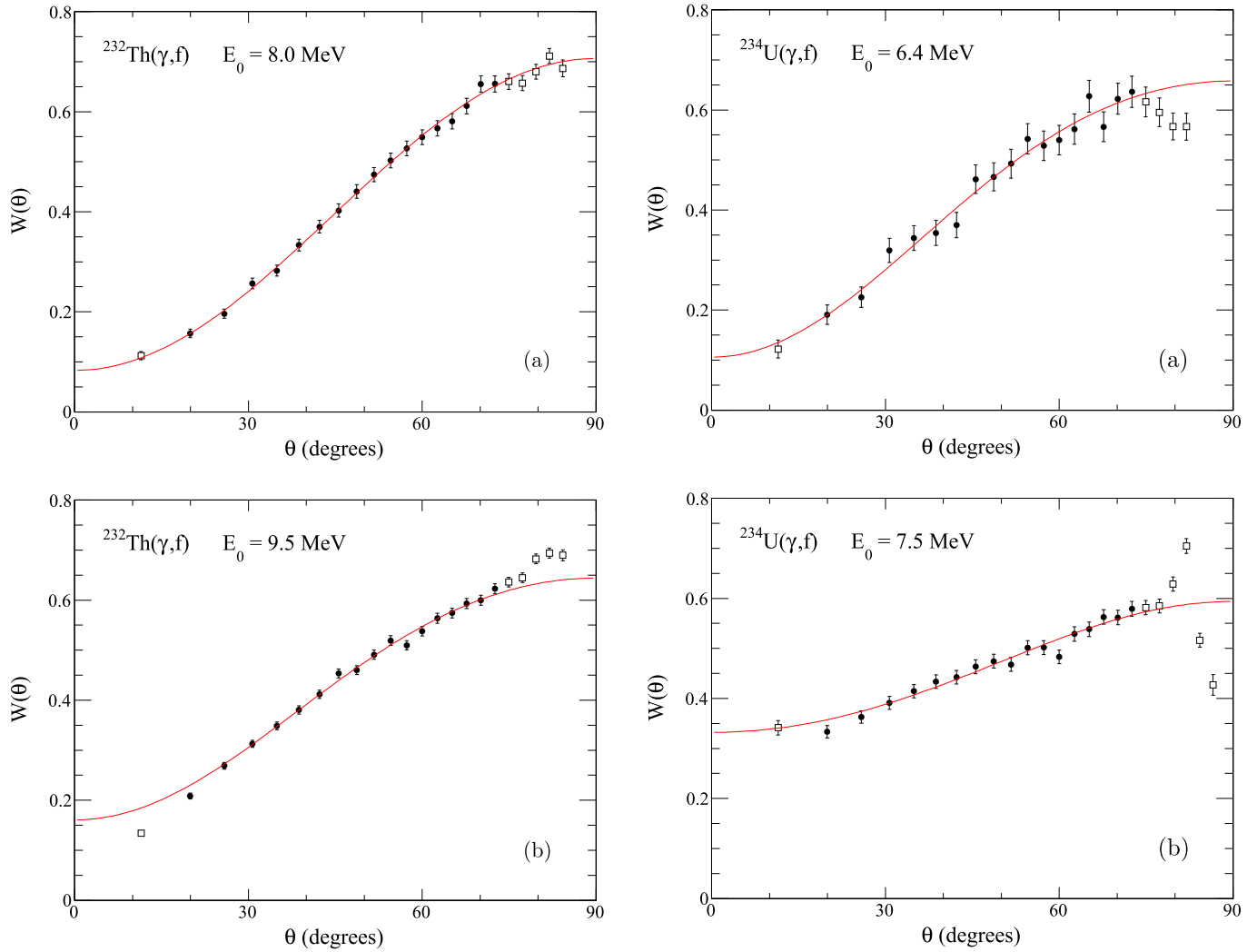


FIG. 8. Fission-fragment angular distribution from $^{232}\text{Th}(\gamma, f)$ at bremsstrahlung endpoint energies $E_0 = 8.0$ MeV (a) and $E_0 = 9.5$ MeV (b). The red line shows the fit of Eq. (8) to the region indicated by the full black circles, the data points visualized by open squares have been omitted from the fit.

paid to the quality of the target that is used, in order to avoid faulty interpretations.

C. Angular distributions

The fission fragment angular distributions were parameterized by the theoretically expected distribution, given by the expression

$$W(\theta) = A + B \sin^2 \theta + C \sin^2 2\theta, \quad (8)$$

which is normalized according to $\int_0^\pi W(\theta) \sin \theta d\theta = 1$. Prior to the parametrization the obtained angular distribution is divided by the angular distribution determined for the α particle activity of the sample, in order to minimize systematic errors that may occur due to the response function for the drift-time to $\cos \theta$ conversion. Angles close to 90° with respect to the incident photon beam direction are excluded from the fit, since these data are influenced by absorption and scattering

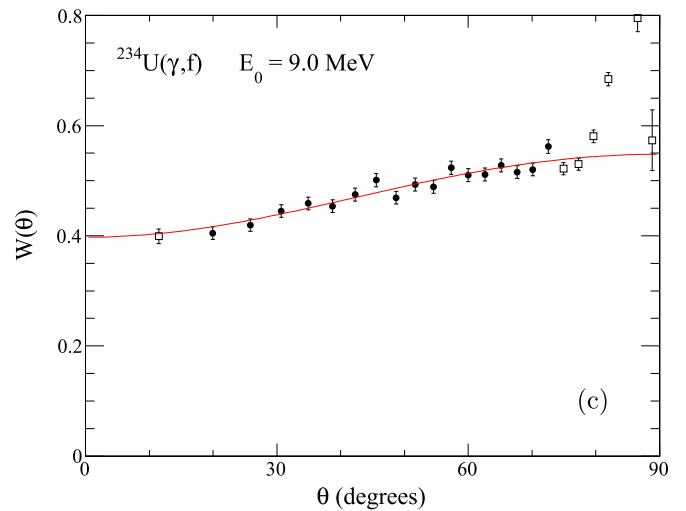


FIG. 9. Fission-fragment angular distribution from $^{234}\text{U}(\gamma, f)$ at bremsstrahlung endpoint energies $E_0 = 6.4$ MeV (a), $E_0 = 7.5$ MeV (b), and $E_0 = 9.0$ MeV (c). The red line shows the fit of Eq. (8) to the region indicated by the full black circles, the data points visualized by open squares have been omitted from the fit.

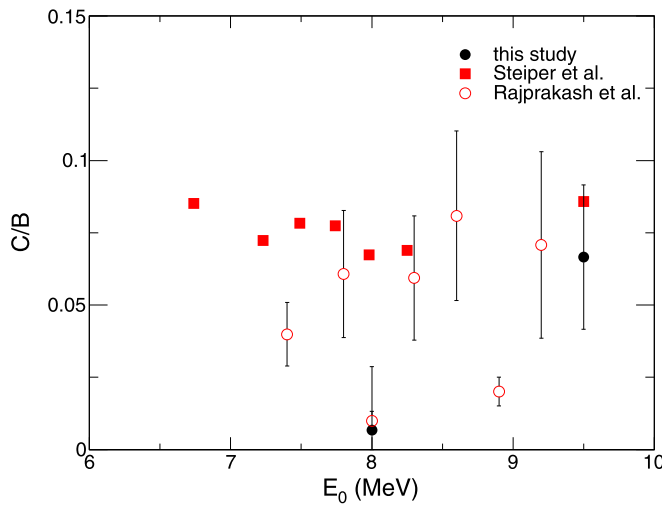
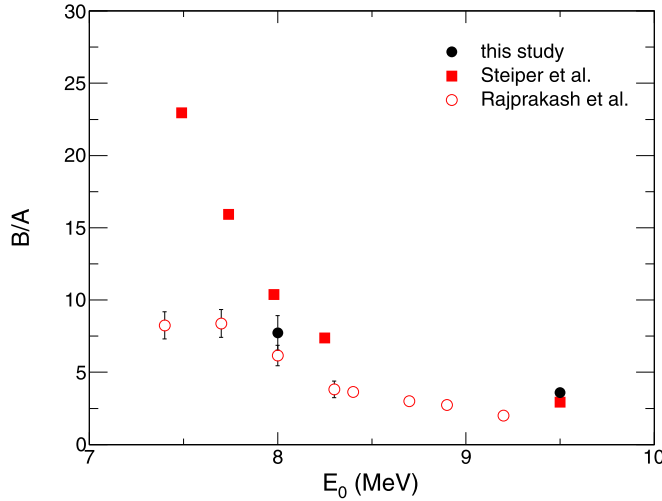


FIG. 10. $^{232}\text{Th}(\gamma, f)$ angular distribution parameter ratios as a function of the bremsstrahlung end-point energy in comparison with literature data [3,33].

effects in the target. Angles close to 0° are also excluded, due to the uncertainty introduced at this angle by the limited angular resolution. The determined angular distributions are displayed in Figs. 8 for $^{232}\text{Th}(\gamma, f)$ and 9 for $^{234}\text{U}(\gamma, f)$. The experimental data is well described by the fit to Eq. (8), represented by the solid red line. The dependence of the angular distribution parameters on the bremsstrahlung endpoint energy for ^{232}Th is compared to data from Refs. [3,33] in Fig. 10. An increasing anisotropy, measured by the ratio B/A , when decreasing the bremsstrahlung endpoint energy, is evident. This behavior is expected for all even-even actinide nuclei within the transition state concept, due to a more predominant fission through the lower energy $(J^\pi, K) = (1^-, 0)$ channel [34]. A sizable quadrupole contribution, measured by the C/B ratio, is only expected if the outer barrier is small compared to the inner one. In the case of ^{232}Th the relative quadrupole contribution is expected to be small and independent from the endpoint energy, according to the systematics of the double-humped fission barrier [35]. As observed in Fig. 10 the experimental data confirms the expectation. The angular distributions in

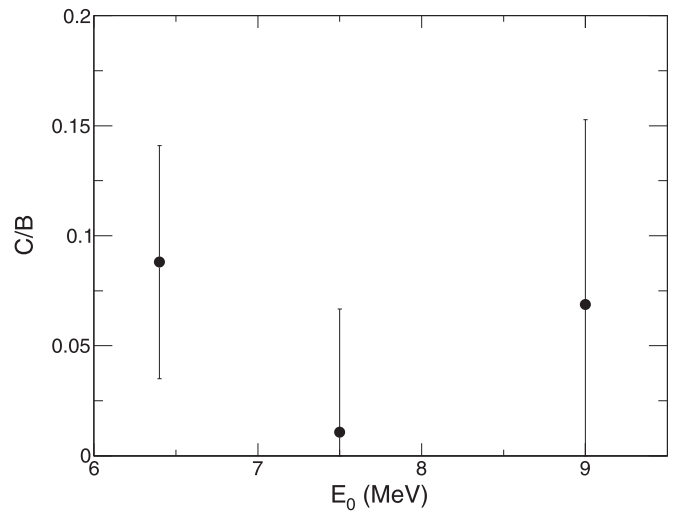
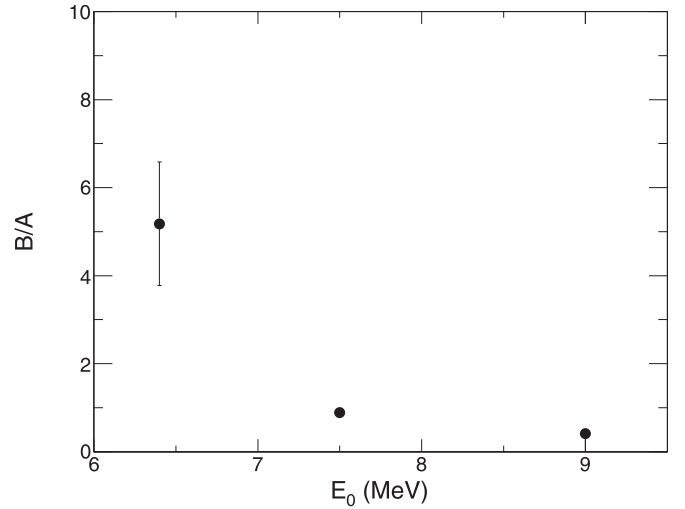


FIG. 11. $^{234}\text{U}(\gamma, f)$ angular distribution parameter ratios as a function of the bremsstrahlung end-point energy from data obtained with a $46.6 \mu\text{g}/\text{cm}^2$ target.

photofission of ^{234}U show similar behavior to those in ^{232}Th , as can be seen in Fig. 11.

D. Mass dependence of angular distributions

In order to investigate a possible mass dependence of the angular distributions, a cut-off parameter M^* is introduced, according to

$$W(\theta, M^*) = \int_{A=M^*}^{\infty} W(\theta, A) dA, \quad (9)$$

where A denotes the heavy-fragment mass number. Similarly, for the TKE dependence a parameter TKE^* is introduced, according to

$$W(\theta, \text{TKE}^*) = \int_{\text{TKE}=\text{TKE}^*}^{\infty} W(\theta, \text{TKE}) d(\text{TKE}). \quad (10)$$

For each value of the parameters M^* and TKE^* the expression in Eq. (8) is fitted to the resulting angular distribution. The result of applying this procedure to the $^{232}\text{Th}(\gamma, f)$ data at $E_0 = 9.5 \text{ MeV}$ is shown in Fig. 12, and for the $^{234}\text{U}(\gamma, f)$

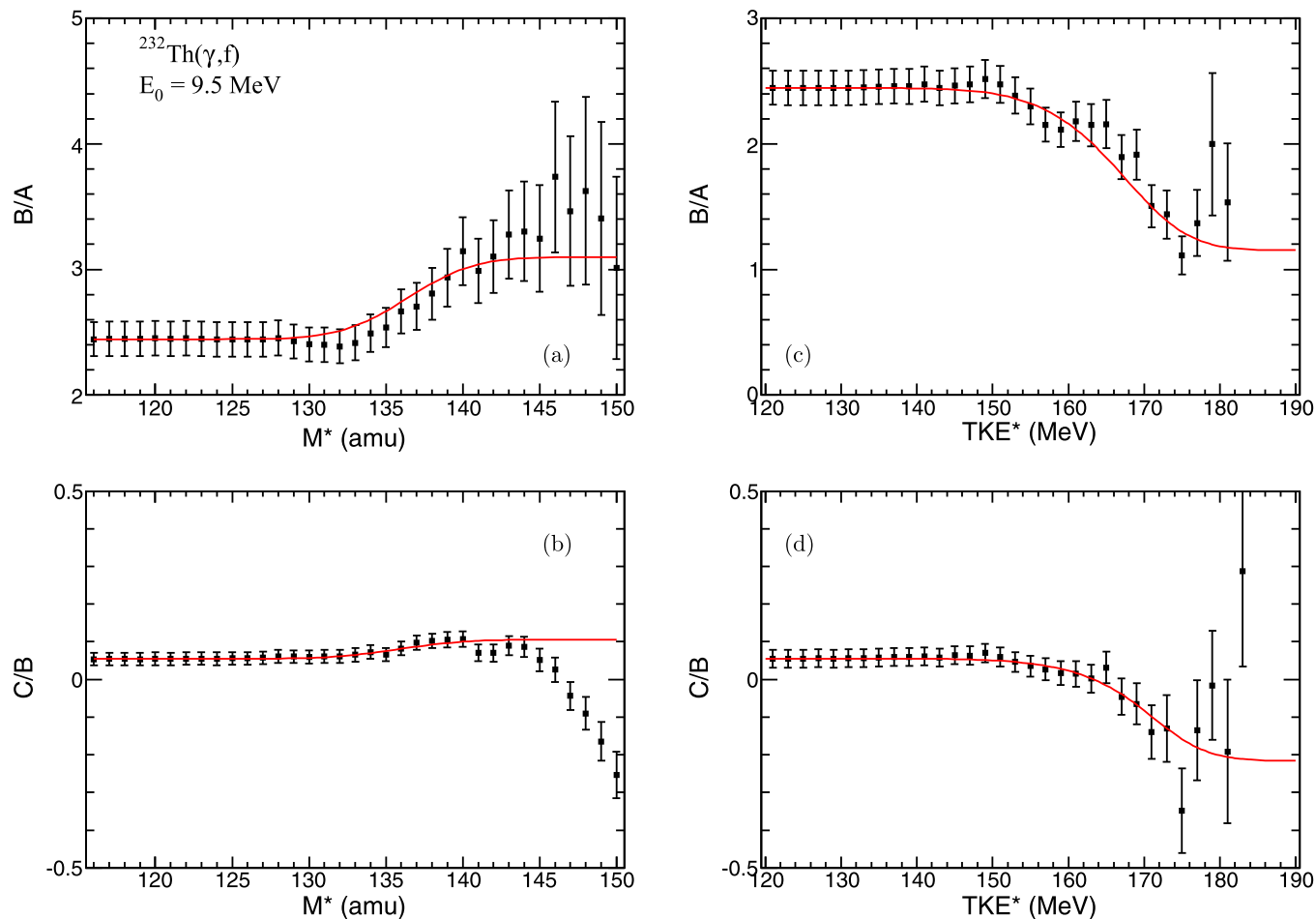


FIG. 12. Dependence of fission-fragment angular distributions in $^{232}\text{Th}(\gamma, f)$ at $E_0 = 9.5$ MeV on the parameters M^* [(a) and (b)] and TKE^* [(c) and (d)], as introduced in Eqs. (9) and (10). The solid red lines show the expected behavior assuming specific angular distributions for the two standard modes.

data at $E_0 = 9.0$ MeV in Fig. 13. In the upper panels an increase in the anisotropy B/A correlated with an increase in M^* is seen for both ^{232}Th and ^{234}U , similarly an increase in the parameter TKE^* is correlated with a decrease in the anisotropy B/A . This forms a consistent picture when keeping the $\langle \text{TKE} \rangle(A)$ dependence in mind. For the asymmetric mass peak, the further away from symmetric mass splits, the lower is the TKE, neglecting the low-yield symmetric component. It is evident that the angular distribution does indeed show a dependence on both the mass and the TKE of the fission fragments. The C/B ratios show more complex behaviors as functions of M^* and TKE^* . The yield of the angular distribution component proportional to $\sin^2 2\theta$ is, however, small for all the experimental data and even takes on negative values for some values of M^* and TKE^* .

A long standing question in multimodal fission is where, in the potential energy landscape, the two standard modes split. According to the calculations by Brosa *et al.* [4], the bifurcation takes place after passing a common outer barrier. On the other hand, there are calculations of the potential energy landscape [36,37] and model calculations to experimental data [38–40] pointing to a bifurcation point in the shape-isomeric

minimum. This results in separate outer barriers for the two standard modes. As mentioned before, a mass (and TKE) dependence of the angular distribution is expected within the MM-RNR model, when separate fission barriers are associated with each mode [41]. Since the yield of each mode has been determined from the fits to Eq. (4), the expected dependence of the angular distribution,

$$\begin{aligned}
 W(A, \text{TKE}, \theta) &= \sum_{m=S1, S2} W_m(\theta) Y_m(A, \text{TKE}) \\
 &= \sum_{m=S1, S2} (A_m + B_m \sin^2 \theta + C_m \sin^2 2\theta) \\
 &\quad \times Y_m(A, \text{TKE}), \tag{11}
 \end{aligned}$$

can be used to calculate the expected dependence of the angular distribution parameters A , B and C on the parameters M^* and TKE^* , as introduced in Eqs. (9) and (10). The yield of the SL mode is very low for all data sets (cf. Tables IV and V), therefore it has been neglected in the following analysis. For each of the angular distribution parameters, one obtains two equations describing their dependence on M^* and TKE^* , respectively. Using the equations describing the dependences

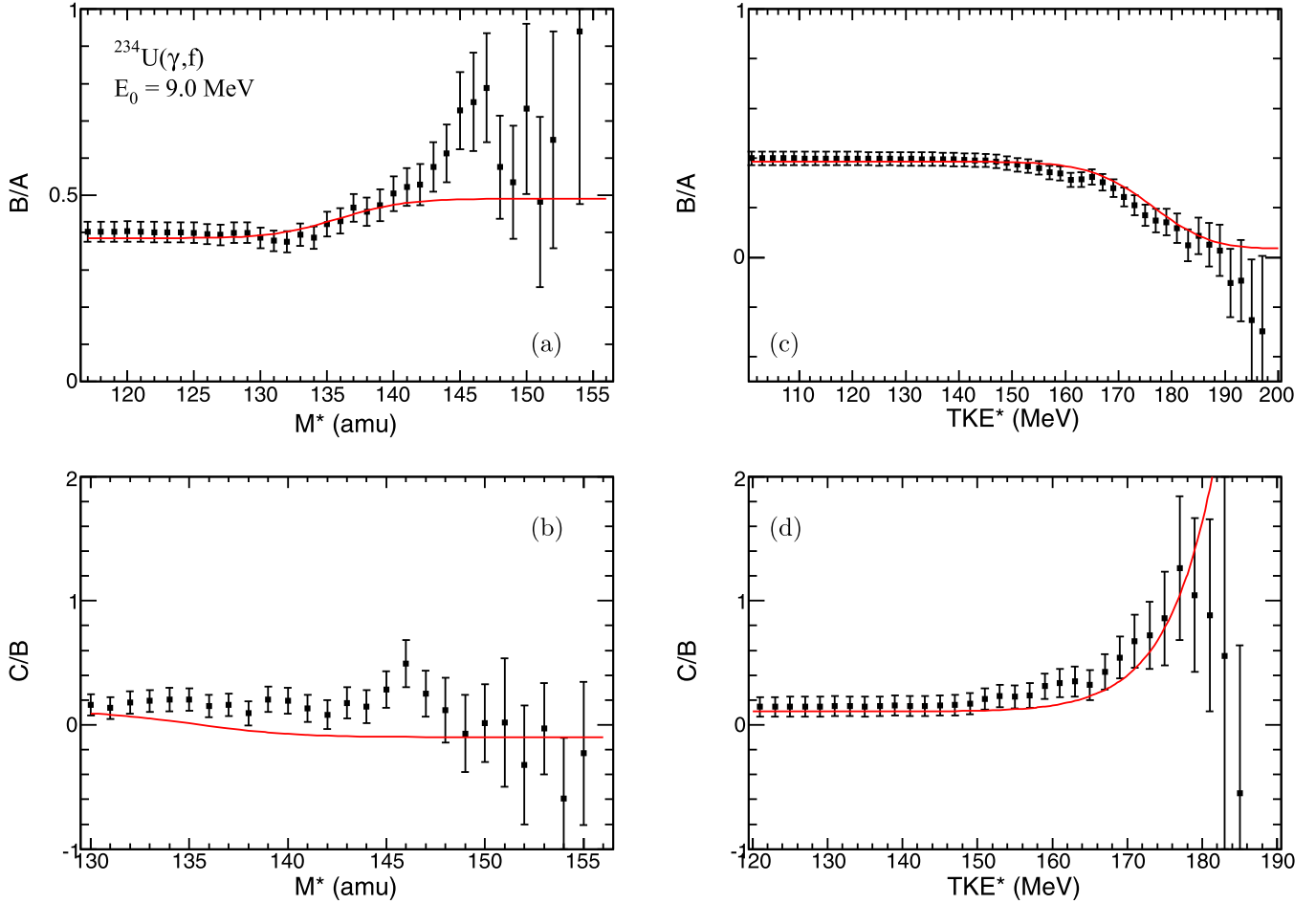


FIG. 13. Dependence of fission-fragment angular distributions in $^{234}\text{U}(\gamma, f)$ at $E_0 = 9.0$ MeV on the parameters M^* [(a) and (b)] and TKE^* [(c) and (d)], as introduced in Eqs. (9) and (10). The solid red lines show the expected behavior assuming specific angular distributions for the two standard modes.

on one of the parameters M^* (or TKE^*), the mode-specific angular distribution parameters A_m , B_m , and C_m can be determined from a fit to the experimental data. If Eq. (11) is valid, the same set of parameters must also describe the dependence on the second of the two parameters TKE^* (or M^*). In Figs. 12 and 13 the behavior according to the fits of A_m , B_m , and C_m is shown by the solid red lines. The fit was performed to the angular distribution dependence on TKE^* , since a stronger dependence was observed there. The mode-specific angular distribution parameters were determined in such a way that the fit function exactly reproduces the parameters obtained when all experimental data is included ($TKE^* = 0$). The predicted dependence of the angular distributions on M^* does indeed describe the data quite well, in particular the ratio B/A , which is sensitive to the outer fission-barrier penetrability. The more complex behaviors as functions of M and TKE observed for the C/B ratios are not as well described, this has not been fully understood but may point at contributions beyond mode-specific angular distributions. Deviations in the B/A and C/B ratio might arise due to the decreasing statistical accuracy with increasing values of M^* and TKE^* , and due to errors in the assumed mass and TKE distributions of the two modes.

The ratio B/A of the angular distribution coefficients determined for the two standard modes in $^{232}\text{Th}(\gamma, f)$ and

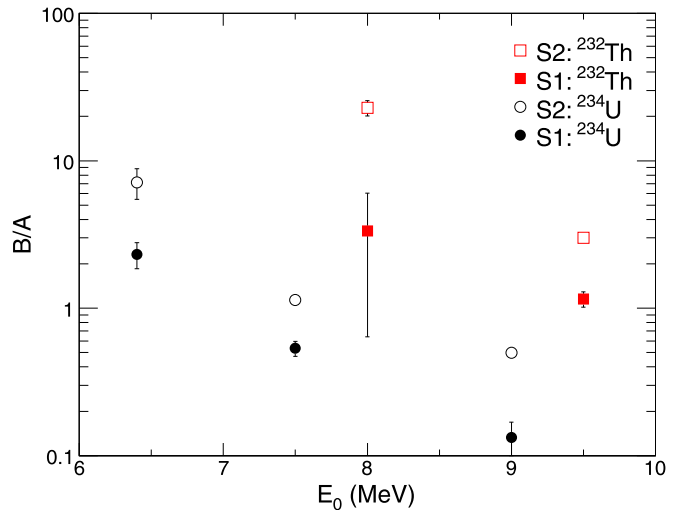


FIG. 14. Ratios B/A of the angular distribution coefficients determined for the two standard fission modes in $^{234}\text{U}(\gamma, f)$ and $^{232}\text{Th}(\gamma, f)$ as a function of the bremsstrahlung end-point energy.

$^{234}\text{U}(\gamma, f)$ are plotted as function of the bremsstrahlung endpoint energy in Fig. 14. The uncertainties in these ratios take into account the uncertainties in the fitted dependence and the uncertainties in the angular distribution parameters when all experimental data is included ($\text{TKE}^* = 0$). In a static model of the potential energy landscape the outer barrier penetrability of the S2 mode is larger than that of the S1 mode, since the relative contribution of the S2 mode to the fission yield is predominant throughout the actinide region of nuclei. With a larger barrier penetrability for the S2 mode a lower value of the B/A ratio is expected. More excitation energy available on top of the barrier would lead to less predominant fission through the lower energy $(J^\pi, K) = (1^-, 0)$ channel. This was not observed in the experimental data. On the contrary, a higher value of the B/A ratio has been found for the S2 mode in all the measurements.

IV. CONCLUSIONS

Correlated fission-fragment mass, energy and angular distributions from bremsstrahlung induced fission of ^{234}U and ^{232}Th have been determined. The findings on mass, and energy distributions from $^{234}\text{U}(\gamma, f)$ contradict our previous experimental results. An explanation for this discrepancy was found in the difference in the thickness of the targets used for the two experiments.

Mass and TKE dependence of the angular distribution of fission fragments in the photofission of ^{234}U and ^{232}Th have been found. The dependence is similar to the mass dependence at higher excitation energies in ^{232}Th , reported in Ref. [3]. The dependence takes the form of an increased anisotropy for far-asymmetric mass splits. The angular distribution dependence

on mass and TKE has also been analysed in terms of fission modes, and could be described as a superposition of specific angular distributions for the two standard fission modes. This analysis results in a larger anisotropy for the S2 mode, as compared to the S1 mode, which suggests a smaller outer barrier penetrability for this fission mode, in contrast to what is expected from the relative yield of the two standard modes in a static model of the fission process. Evidence for or against the conjecture of separate outer fission barriers of the two standard modes may be found by extending the experiments to lower bremsstrahlung endpoint energies, in order to extract barrier parameters for the different fission modes from their respective angular distributions.

ACKNOWLEDGMENTS

We thank the dedicated staff at the S-DALINAC for providing the beam. This work was supported in part by Deutsche Forschungsgemeinschaft (Contract No. SFB634), the German Bundesministerium für Bildung und Forschung (Contract No. 05P15RDENA), the Hessisches Ministerium für Wissenschaft und Kunst (LOEWE Center HIC for FAIR), and the cooperation agreement between GSI Helmholtzzentrum für Schwerionenforschung and Technische Universität Darmstadt. One of the authors (A.O.) acknowledges the support from the Extreme Light Infrastructure Nuclear Physics (ELI-NP) Phase II, a project cofinanced by the Romanian Government and the European Union through the European Regional Development Fund—the Competitiveness Operational Programme (1/07.07.2016, COP, ID 1334), with which this work was finalized.

-
- [1] A. Bohr, in *Proceedings of the International Conference on Peaceful Uses of Atomic Energy, Geneva, 1955* (United Nations, New York, 1956), Vol. 1, p. 151.
- [2] W. Wilke, R. Heil, U. Kneissl, U. Seemann, F. Steiper, H. Stöher, and T. Weber, *Phys. Lett. B* **207**, 385 (1988).
- [3] F. Steiper, T. Frommhold, W. Henkel, A. Jung, U. Kneissl, and R. Stock, *Nucl. Phys. A* **563**, 282 (1993).
- [4] U. Brosa, S. Grossmann, and A. Müller, *Phys. Rep.* **197**, 167 (1990).
- [5] A. Richter, in *Proceedings of the 5th European Particle Accelerator Conference 1996*, edited by S. Myers *et al.* (Institute of Physics Publishing, Bristol and Philadelphia, PA, 1996), p. 110.
- [6] A. Göök, M. Chernykh, C. Eckardt, J. Enders, P. von Neumann-Cosel, A. Oberstedt, S. Oberstedt, and A. Richter, *Nucl. Phys. A* **851**, 1 (2011).
- [7] P. Mohr, J. Enders, T. Hartmann, H. Kaiser, D. Schiesser, S. Schmitt, S. Volz, F. Wissel, and A. Zilges, *Nucl. Instrum. Methods A* **423**, 480 (1999).
- [8] K. Sonnabend, D. Savran, J. Beller, M. Büssing, A. Constantinescu, M. Elvers, J. Endres, M. Fritzsche, J. Glorius, J. Hasper, J. Isaak, B. Löher, S. Müller, N. Pietralla, C. Romig, A. Sauerwein, L. Schnorrenberger, C. Wälzlein, A. Zilges, and M. Zweidinger, *Nucl. Instrum. Methods A* **640**, 6 (2011).
- [9] C. Budtz-Jørgensen, H.-H. Knitter, C. Straede, F.-J. Hamsch, and R. Vogt, *Nucl. Instrum. Methods A* **258**, 209 (1987).
- [10] F. Tovesson, F.-J. Hamsch, S. Oberstedt, and H. Bax, *J. Nucl. Sci. Technol.* **39**, 673 (2002).
- [11] V. A. Khryachkov, I. V. Dunaeva, M. V. Dunaev, N. N. Semenova, and A. I. Sergachev, *Instrum. Exp. Tech.* **46**, 804 (2003).
- [12] O. Bunemann, T. Cranshaw, and J. Harvey, *Can. J. Res. A* **27**, 191 (1949).
- [13] A. Göök, M. Chernykh, J. Enders, A. Oberstedt, and S. Oberstedt, *Nucl. Instrum. Methods A* **621**, 401 (2010).
- [14] S. Agostinelli *et al.*, *Nucl. Instrum. Methods A* **506**, 250 (2003).
- [15] A. S. Soldatov, *Yad. Konstany* **1**, 859 (1997).
- [16] M. Chadwick, P. Oblozinsky, M. Herman, N. Greene, R. McKnight, D. Smith, P. Young, R. MacFarlane, G. Hale, S. Frankle, A. Kahler, T. Kawano, R. Little, D. Madland, P. Moller, R. Mosteller, P. Page, P. Talou, H. Trellue, M. White, W. Wilson, R. Arcilla, C. Dunford, S. Mughabghab, B. Pritychenko, D. Rochman, A. Sonzogni, C. Lubitz, T. Trumbull, J. Weinman, D. Brown, D. Cullen, D. Heinrichs, D. McNabb, H. Derrien, M. Dunn, N. Larson, L. Leal, A. Carlson, R. Block, J. Briggs, E. Cheng, H. Huria, M. Zerkle, K. Kozier, A. Courcelle, V. Pronyaev, and S. van der Marck, *Nucl. Data Sheets* **107**, 2931 (2006).
- [17] S. Pommé, E. Jacobs, M. Piessens, D. De Frenne, K. Persyn, K. Govaert, and M.-L. Yoneama, *Nucl. Phys. A* **572**, 237 (1994).
- [18] J. Lindhard, V. Nielsen, M. Scharff, and P. V. Thomsen, K. Dan. Vidensk. Selsk. Mat. Fys. Medd. **33**(10), 1 (1963).

- [19] J. Lindhard, M. Scharff, and H. E. Schiøtt, *K. Dan. Vidensk. Selsk. Mat. Fys. Medd.* **33**(14), 1 (1963).
- [20] M. Piessens, Proefschrift, Rijksuniversiteit Gent, 1989.
- [21] V. F. Apalin, Yu. N. Griityuk, I. E. Kutikov, V. I. Lebedev, and L. A. Mikaelian, *Nucl. Phys.* **71**, 553 (1965).
- [22] G. Barreau, A. Sicre, F. Caitucoli, M. Asghar, T. Doan, B. Leroux, G. Martinez, and T. Benfoughal, *Nucl. Phys. A* **432**, 411 (1985).
- [23] J. Randrup and P. Möller, *Phys. Rev. Lett.* **106**, 132503 (2011).
- [24] K.-H. Schmidt, S. Steinhäuser, C. Böckstiegel, A. Grewe, A. Heinz, A. R. Junghans, J. Benlliure, H.-G. Clerc, M. de Jong, J. Müller, M. Pfützner, and B. Voss, *Nucl. Phys. A* **665**, 221 (2000).
- [25] F. James, CERN Program Library Long Writeup D506, CERN Computing and Networks Division, 1998.
- [26] F. James and M. Winkler, computer code MINUIT2, CERN Computing and Networks Division, 2008.
- [27] B. D. Wilkins, E. P. Steinberg, and R. R. Chasman, *Phys. Rev. C* **14**, 1832 (1976).
- [28] F.-J. Hamsch, H.-H. Knitter, C. Budtz-Jørgensen, and J. P. Theobald, *Nucl. Phys. A* **491**, 56 (1989).
- [29] E. Birgersson, A. Oberstedt, S. Oberstedt, and F.-J. Hamsch, *Nucl. Phys. A* **817**, 1 (2009).
- [30] C. Wagemans, P. Schillebeeckx, and A. Deruytter, *Nucl. Phys. A* **502**, 287c (1989).
- [31] J. Ziegler, M. Ziegler, and J. Biersack, computer code SRIM 2008.04, 2008.
- [32] J. F. Ziegler, *Appl. Phys. Lett.* **31**, 544 (1977).
- [33] H. G. Rajprakash, G. Sanjeev, K. B. Vijaykumar, K. Siddappa, B. K. Nayak, and A. Saxena, *Indian J. Phys.* **83**, 1135 (2009).
- [34] E. Jacobs and U. Kneissl, in *The Nuclear Fission Process*, edited by C. Wagemans (CRC Press, Boca Raton, FL, 1991).
- [35] R. Vandenbosch, *Phys. Lett.* **45B**, 207 (1973).
- [36] P. Siegler, F.-J. Hamsch, S. Oberstedt, and J. Theobald, *Nucl. Phys. A* **594**, 45 (1995).
- [37] S. Oberstedt, F.-J. Hamsch, and F. Vivès, *Nucl. Phys. A* **644**, 289 (1998).
- [38] F.-J. Hamsch, F. Vivès, P. Siegler, and S. Oberstedt, *Nucl. Phys. A* **679**, 32 (2000).
- [39] G. Vladuca, A. Tudora, F.-J. Hamsch, and S. Oberstedt, *Nucl. Phys. A* **707**, 32 (2002).
- [40] F.-J. Hamsch, G. Vladuca, A. Tudora, S. Oberstedt, and I. Ruskov, *Ann. Nucl. Energy* **32**, 1297 (2005).
- [41] H.-H. Knitter, in *The Nuclear Fission Process*, edited by C. Wagemans (CRC Press, Boca Raton, FL, 1991).